



## Spatially resolved acoustic spectroscopy for selective laser melting



Richard J. Smith<sup>a</sup>, Matthias Hirsch<sup>b</sup>, Rikesh Patel<sup>a</sup>, Wenqi Li<sup>a</sup>, Adam T. Clare<sup>b,\*</sup>, Steve D. Sharples<sup>a</sup>

<sup>a</sup> Advanced Optics Group, Faculty of Engineering, The University of Nottingham, Nottingham NG7 2RD, UK

<sup>b</sup> Advanced Manufacturing Group, Faculty of Engineering, The University of Nottingham, Nottingham NG7 2RD, UK

### ARTICLE INFO

#### Article history:

Received 16 January 2016

Received in revised form 21 April 2016

Accepted 4 May 2016

Available online 6 May 2016

#### Keywords:

Non-destructive testing  
Spatially resolved acoustic spectroscopy  
Selective laser melting  
Additive manufacture  
Titanium Ti-6Al-4V

### ABSTRACT

Additive manufacturing (AM) is a manufacturing technique that typically builds parts layer by layer, for example, in the case of selective laser melted (SLM) material by fusing layers of metal powder. This allows the construction of complex geometry parts, which, in some cases cannot be made by traditional manufacturing routes. Complex parts can be difficult to inspect for material conformity and defects which are limiting widespread adoption especially in high performance arenas. Spatially resolved acoustic spectroscopy (SRAS) is a technique for material characterisation based on robustly measuring the surface acoustic wave velocity. Here the SRAS technique is applied to prepare additively manufactured material to measure the material properties and identify defects. Results are presented tracking the increase in the measured velocity with the build power of the selective laser melting machine. Surface and subsurface defect measurements (to a depth of  $\sim 24 \mu\text{m}$ ) are compared to electron microscopy and X-ray computed tomography. It has been found that pore size remains the same for 140 W to 190 W melting power (mean: 115–119  $\mu\text{m}$  optical and 134–137  $\mu\text{m}$  velocity) but the number of pores increase significantly (70–126 optical, 95–182 velocity) with lower melting power, reducing overall material density.

© 2016 The Authors. Published by Elsevier B.V. This is an open access article under the CC BY license (<http://creativecommons.org/licenses/by/4.0/>).

### 1. Introduction

Additive manufacturing is a rapidly growing area for complex part manufacture and encompasses a wide variety of different techniques, all of which have the property of additive accumulation of material to form the part. Some of the techniques build parts layer by layer which offers the possibility of integration of the build process with existing inspection techniques. Selective laser melting (SLM) is an additive manufacturing (AM) technique that can produce complex geometrical, 'high value' parts for the aerospace (Abe et al., 2001), tooling (Voet et al., 2005) and medical industry (Melchels et al., 2012). The layer by layer SLM process uses a laser to melt a deposited loose powder layer into a fused object that is then built up by adding more layers (Kruth et al., 2005). This manufacturing approach enables the construction of high complexity parts that, in many cases, cannot be made with traditional manufacturing routes. There are limitations to this technique; the relatively low build speed compared to traditional manufacturing processes means it is currently only economical for low volume, high value, high complexity parts. Additionally, identification of

defects in complex geometry parts is difficult post build and the lack of in-situ NDE methods is preventing the proliferation of this technology (Tapia and Elwany, 2014).

The layer-by-layer nature of the manufacture of the part offers the possibility to inspect the full volume of the part, by inspecting each layer as it is built. This offers the opportunity to characterise defects and check material conformity as each layer is created, feeding back into the build process to i) scrap the build – saving valuable build time and material – or ii) enact an on-the-fly repair to allow completion of the part. Full online volume inspection will revolutionise the AM industry, and give confidence in parts manufactured to ensure they are all within specification.

This remains challenging since there are a number of hurdles to be overcome. Firstly, the NDE techniques used must have the inspection capabilities required; to be able to measure defects, material properties and size conformity. Secondly they must be compatible with the AM build process; the limited chamber size, be safe for routine use, and have sufficient scan speed so as not to unduly affect throughput.

Research towards online in-situ monitoring of AM material is gaining momentum, for example in melt pool temperature monitoring, Islam et al. have shown that a pyrometer/camera combination system can fit inside the build chamber and is capable of determining balling of the powder (steel based in this case) (Islam

\* Corresponding author.

E-mail address: [adam.clare@nottingham.ac.uk](mailto:adam.clare@nottingham.ac.uk) (A.T. Clare).

et al., 2013). Pavlov et al. showed that a pyrometer situated coaxially is capable of detecting the heating and cooling cycle of parts produced in Inconel 625 (Pavlov et al., 2010). It was shown that the signal received by the pyrometer reaches a maximum value at 100  $\mu\text{m}$  layer thickness because the contact between the powder layer and the substrate is lost and hence the laser energy is absorbed fully into the powder. This information can be used in determining if powder has likely melted in order to produce a feature of sufficient integrity. A pyrometry quality measurement system enables monitoring of the melting behaviour of the powder but not the direct evaluation of part integrity.

Optical systems have also been used for melt pool analysis in SLM manufacture. Kruth et al. (Kruth et al., 2007) have shown this with a coaxial CMOS camera and a photodiode system that is capable of interrogating the melt pool. Their system could dynamically adjust the laser power according to varying thermal conductivity areas within the build (such as overhangs). A camera based system, with high speed image processing at a sample rate of 10–20 kHz has been shown to be capable of interrogating the whole build and distinguish between fused powder and pores with a range of materials at a pixel size of 100  $\mu\text{m}$   $\times$  100  $\mu\text{m}$  (Clijsters et al., 2014). X-ray computed tomography (XCT), although it has not been implemented as an in-situ NDE method for AM, has shown promise in the three-dimensional measurement of parts produced with metal powder AM techniques. In work by Zhou et al., it has been shown that a full reconstruction of defects in 3D space is possible (Zhou et al., 2015) and correlates well with destructively prepared samples and SEM analysis. Furthermore, Tamas-Williams et al. have shown that XCT measurements of selective electron beam melted (SEBM) samples give confidence of detection down to a size limit of  $\sim 5 \mu\text{m}$  (Tamas-Williams et al., 2015). XCT analysis of bulk defects has been shown to be very useful; however, its use for near surface defects can be problematic due to degradation of the signal.

Laser ultrasound has been used for offline inspection of artificial defects in machined plates of Ti-6Al-4V and artificial defects in laser powder deposited parts of the same materials (Nemeth et al., 2005). In this work Nemeth et al. have demonstrated the capability of their Time of Flight measurements to localise blind holes created artificially by electron beam machining. In more recent work, Rudlin et al. (Rudlin et al., 2014) compared laser ultrasound inspection with laser thermography and eddy current analysis to look for manufactured defects in laser deposited material. Utilising the same offline instrument system Cerniglia et al. (Cerniglia et al., 2013) inspected material for manufactured flaws and discussed the need for automatic feature detection from the acoustic data to aid with defect classification. The only acoustic online inspection system reported comes from the use of a bulk wave piezoelectric transducer embedded in the build plate of an SLM machine (Rieder et al., 2014). Rieder et al. showed changes in the acoustic signal as the part (a cylinder to match the geometry of the transducer) was built. It was possible to monitor the change in thickness as layers were added by tracking the back wall echo location. Also, if defects were present additional echoes could be observed. This shows how useful online acoustic measurements could be, however with a single transducer in the build plate there is no spatial information obtained about the sample limiting its usefulness to samples with very simple geometries.

This paper introduces an inspection method, spatially resolved acoustic spectroscopy (SRAS), which can be used for material characterisation and defect detection for AM parts (Clark et al., 2011). SRAS uses surface acoustic waves (SAWs) to probe the material to a depth of a few 10's or 100's  $\mu\text{m}$ . This yields information about the material microstructure and defects at the surface and near sub surface.

The SRAS instrument has been described in detail elsewhere (Smith et al., 2014) so will only be described briefly here. A

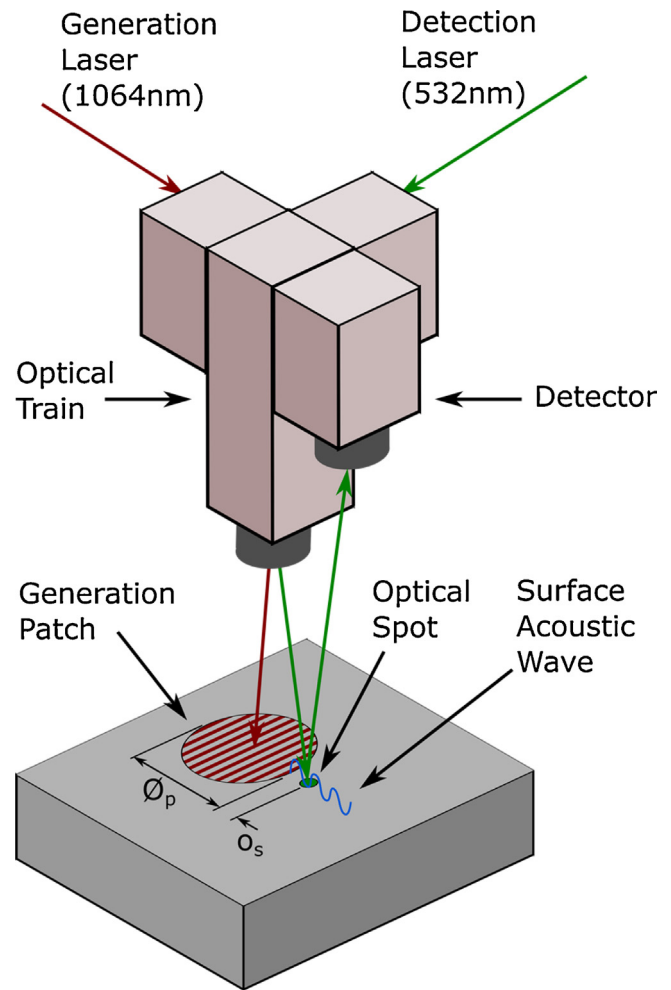


Fig. 1. Schematic showing the important features of the SRAS instrument, including, the pulsed generation laser, the projection mask, the continuous wave detection laser and detector.

schematic of the instrument is shown in Fig. 1. A pulsed laser passes through a chrome grating and is imaged to the sample surface, where the absorbed pulses thermoelastically generate acoustic waves. The wavelength of the surface acoustic wave is defined by the spacing of the lines on the grating and so the waves have a characteristic frequency  $f$  defined by  $f = v/\lambda$ , where  $v$  is the SAW velocity of the material under the generation patch ( $\phi_p$ ) and  $\lambda$  is the acoustic wavelength. This frequency is measured by monitoring the interaction of the acoustic waves with a probe laser (at distance  $o_s$ ), and is then processed to recover the velocity. The sample is raster scanned to build up an image. The SAW velocity varies with grain orientation giving information about the grain size and orientation distribution. If multiple velocity images are taken with different acoustic wave propagation directions then it is possible to recover the actual orientation of the grains (Li et al., 2012). The choice of grating spacing and generation patch area defines the working frequency and the spatial resolution of the instrument, these are typically 100–150 MHz and 100  $\mu\text{m}$  respectively. However, measurements from 5 MHz–300 MHz and with resolutions from 1 mm down to 25  $\mu\text{m}$  have been performed previously.

SRAS is a good candidate for inspection of SLM parts. Firstly, the depth sensitivity of SRAS can be adjusted in order to be sensitive to material over different depths. This is achieved by changing the acoustic wavelength which can be adjusted by modifying the line spacing of the projection grating allowing the inspection of a single or several build layers at once. Secondly, the scanning speed is fast,

and is ultimately limited by the laser repetition rate. The current version of the instrument uses a 2 KHz repetition rate for the laser, leading to ~1000 points per second after data acquisition dead time and scanning overheads are included. Achieved scanning speeds will be discussed in the Results and Discussion section. Thirdly, the all optical nature of the instrument presents an opportunity to miniaturise the instrument significantly to make the instrument compatible with the restrictions imposed by SLM build chambers.

This paper demonstrates offline inspection of polished SLM material produced with different build parameters and shows how the changing parameters affect the measured acoustic velocity. The detection of typical SLM defects, both at the surface and sub-surface is also demonstrated. Finally, the challenges to overcome for online inspection are explored in detail.

## 2. Methodology

### 2.1. Samples

A series of SLM specimens were produced for inspection with the SRAS instrument system. The manufacture of the test specimens followed standard SLM build process which will now be described. The material used was a Titanium alloy powder of type Ti-6Al-4V in grade 23-5. The powder has a size range of 15–45  $\mu\text{m}$  with >50% of the powder being below 31.6  $\mu\text{m}$ , measured with a laser diffractometer particle size analyser, a Malvern Mastersizer 3000.

The selective laser melting apparatus used in this study is a Renishaw AM 250 containing a continuous wave Ytterbium fibre laser (wavelength of 1070 nm) that can output a maximum power of 200 W in continuous mode. The intensity distribution across the laser spot is assumed to be Gaussian. The laser beam diameter is defined as 70  $\mu\text{m}$  at the powder interface and the maximum scanning speed is defined as 2000  $\text{mms}^{-1}$ .

All specimens are 10  $\times$  10  $\times$  10 mm in size with a layer thickness ( $t$ ) of 30  $\mu\text{m}$  as this provides a good compromise between build quality (i.e. roughness optimisation) and production speed. In order to assess a change in defect occurrence and defect creation frequency, the laser power has been adjusted in steps of 10 W starting from 70 W to 200 W. The scanning speed (600  $\text{mms}^{-1}$ ) and hatch spacing (75  $\mu\text{m}$ ) remained constant throughout the build process. A meander scan strategy (rotation of 67°) was employed for the production of the test pieces and is depicted in Fig. 2(a).

Since the SLM process builds samples in a three dimensional fashion, volumetric energy input,  $E$  ( $\text{J}/\text{mm}^3$ ), is chosen to describe the energy flow into the system. This parameter is a key factor in determining the quality of the build as it dictates the capability of the laser to melt the material completely. The equation is described by:

$$E = \frac{P}{v_{SLM}ht}$$

where  $P$  (W) is the laser power,  $v_{SLM}$  is the scan speed (mm/s),  $h$  is the hatching space (mm) and  $t$  is the layer thickness (mm). The specific energy necessary to produce dense parts (>99%) varies with the powdered material used. A summary of the processing information for each sample is shown in Table 1. The input power was chosen as suitable parameter to vary as studies have shown that identical energy densities have resulted in dissimilar material responses due to a variation in cooling time associated with scan speed, spot size and laser power (Islam et al., 2013; Niebling et al., 2002).

### 2.2. Polishing of samples for analysis

After SLM manufacture the samples were polished prior to inspection by the SRAS instrument as the current detector requires a specular reflection from the sample surface. The surface was prepared by grinding and polishing to leave a surface finish that gave a good specular reflection for optimum operation of the detector. The samples were polished on the bottom surface only in the build direction shown in Fig. 2(b); this allows the other surfaces free for future comparison once optically rough surface detection capabilities are available in the instrument.

### 2.3. SRAS scan details

Each sample was scanned using the SRAS instrument. The generation laser is a Q-switched laser (AOT-YAG-10Q) which emits 1–2 ns pulses at a repetition frequency of 1–6.25 kHz. The probe laser is a 532 nm continuous wave laser (Laser Quantum Torus 532). The acoustic wavelength was ~24  $\mu\text{m}$  and the generation patch size on the sample was ~200  $\mu\text{m}$ . This leads to a depth sensitivity of ~24  $\mu\text{m}$  and a spatial resolution of the order of 100  $\mu\text{m}$ . The instrument acquires a waveform for each pulse of the generation laser, and these are processed to produce the images shown in the results section. Each pixel in the velocity map is the result of a single laser pulse, there is no averaging, and the velocity noise is typically ~15m/s (0.5%). The scan size was 10  $\times$  10 mm with a pixel size of 25  $\times$  25  $\mu\text{m}$ , the data was captured at the laser repetition rate of 2000 points per second but due to the time required to move the sample and read out the data the final data acquisition rate was approximately 650 points per second.

Additionally, higher resolution scans were performed on sample 6 (140 W) and sample 10 (190 W), for these scans the pixel size was reduced to 5  $\times$  5  $\mu\text{m}$  to allow defects to be investigated in more detail.

To assess the surface condition sample 6 (140 W) and sample 10 (190 W) were imaged with a Hitachi TM3030 scanning electron microscope (SEM). Secondary Electron (SE) micrographs were taken at 20 kV with different magnifications to highlight pore defects of the same surfaces investigated with SRAS. The resulting micrographs were analysed and compared with the SRAS data.

For comparison of sub surface defects with the SRAS data, sample 6 (140 W) and sample 10 (190 W) were measured with an XRADIA Versa XRM-500 3D X-ray microscope. The exposure time was set to 1.5 s at 0.45° increments and the source voltage was 160 kV. The pixel resolution of the reconstructed images was 14.696  $\mu\text{m}$ . Analysis of the data was conducted with Avizo 8.1, where a top-hat filtering step (Sim et al., 2008) was used for uniform thresholding of the three dimensional data. The extrapolated XCT defect data has then been used to compare with the SRAS scans. The X-ray signal deteriorates at the edge of a sample, which affects the specific sizing of the pores that can be detected near the surface. For the purposes of this paper, the XCT is used to compare pore locations and rough shape descriptors only.

## 3. Results and discussion

The experiment data was analysed in two ways, firstly to look at changes in the material properties with changes in the build parameters and secondly to assess the ability of SRAS to detect surface and subsurface defects.

### 3.1. Material properties with different build powers

Fig. 3 shows the data obtained from a scan of the 170 W SLM sample, Fig. 3(a) shows the optical image which is a by-product of the SRAS scan, this image is the record of the DC light level of



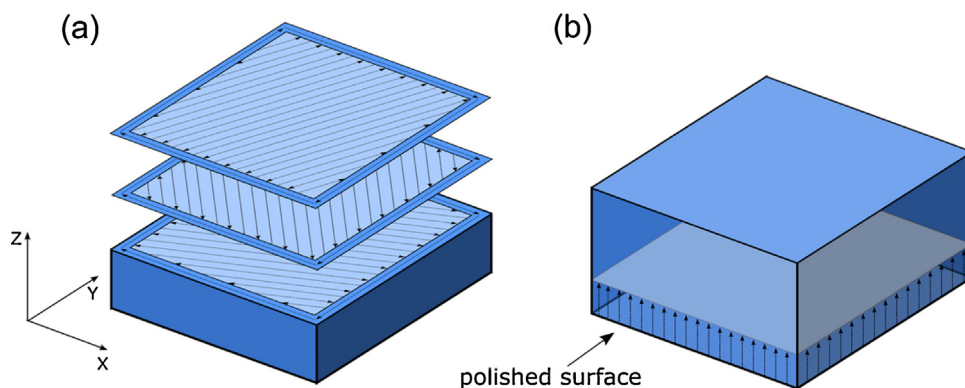


**Fig. 2.** (a) A schematic of the SLM specimen laser scan strategy with skin scan and parallel meander scan ( $67^\circ$  rotation from layer to layer) and (b) polishing direction indication used for SRAS analysis.

**Table 1**  
SLM processing parameters used for this study.

Sample ID	1	2	3	4	5	6	7	8	9	10	11
Laser Power (W)	70	80	90	120	130	140	160	170	180	190	200
Energy input, $E$ ( $10^{-9} \text{Jm}^{-3}$ )	51.9	59.3	66.7	88.9	96.3	103.7	118.5	125.9	133.3	140.7	148.1

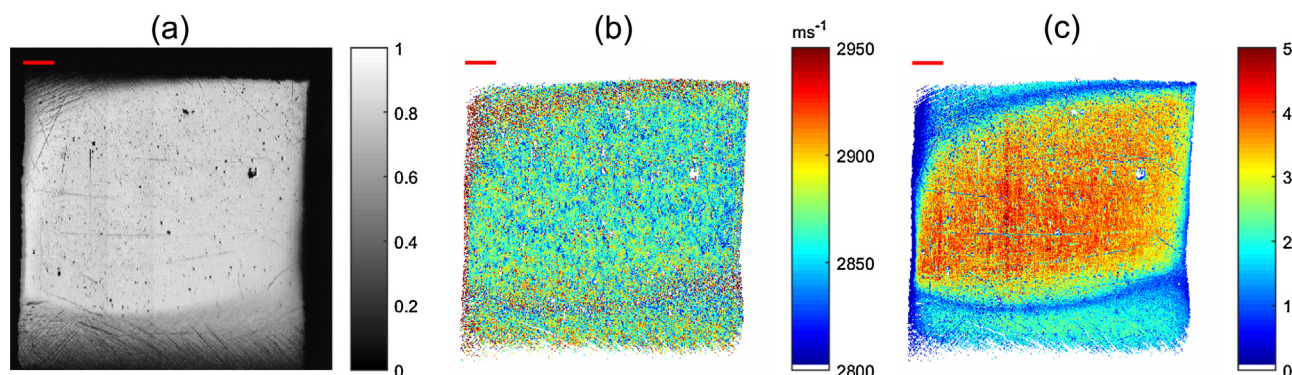


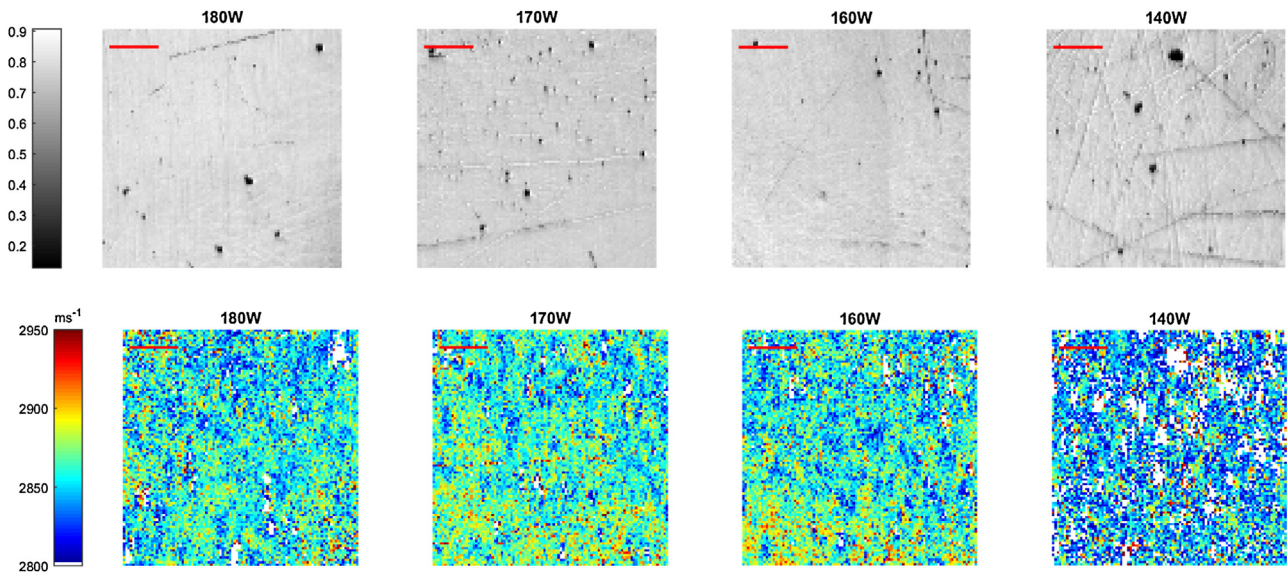
**Fig. 3.** Example measurement data for sample 8 (170W), (a) the optical image shows a large flat region in the centre which is used for analysis, also note surface pores are visible, (b) the velocity map showing typical macrozone structure of titanium, (c) image showing the amplitude of the acoustic signal. Scale bar 1 mm.

the probe laser beam at each position of the sample. The resolution of this optical image is related to the focal spot size of the probe beam on the sample and is  $\sim 5 \mu\text{m}$ . The optical image shows dark marks on the sample surface which are either surface pores or residual surface scratches from the polishing process. The central region is flat and provides uniform light level return for the SRAS scan. Fig. 3(b) shows the velocity map produced from the acoustic data, the central region where the surface is flat, shows the typical macrozone structure of a fine grained titanium sample, the mean velocity is 2860m/s with textural variation of  $\pm 50$  m/s. For a single grain the velocity varies with crystallographic orientation by  $\pm 250$  m/s for this titanium alloy, the observed variation is lower as the average velocity is measured for the grain population underneath the patch. Variations in the grain orientation distribution lead to regions with slightly faster or slower mean velocities. The size and variation of these zones over sample is a useful indicator of the material uniformity. For the surface measured the grain size is expected to be much smaller than our patch size in the X-Y plane with a high aspect ratio in the Z plane ( $\sim 60 \mu\text{m}$ ) (Simonelli et al., 2014) due to the heat sink effect of the build plate at this surface leading to rapid cooling of the material. Fig. 3(c) is an image of the acoustic amplitude and shows high signal strength in the central zone. This map, as well as the optical map, can be used to remove 'poor' quality points from the velocity image. For example, if mea-

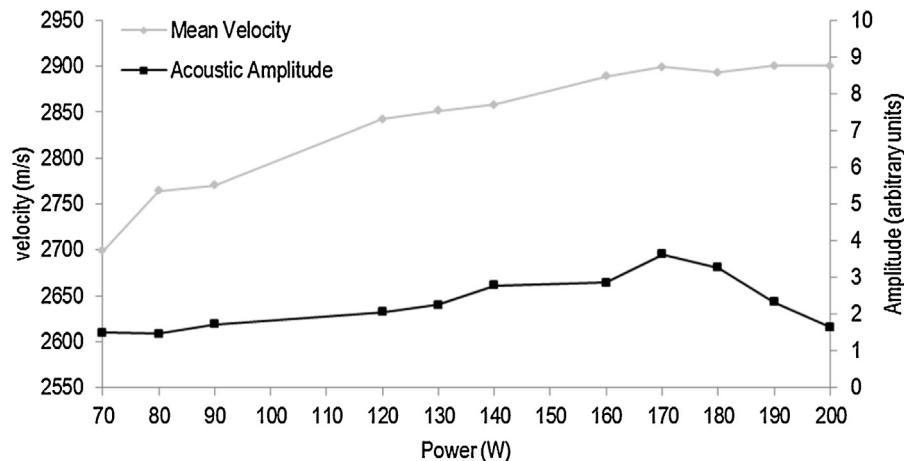
surement point does not meet the required acoustic amplitude or optical return level the velocity for this point is not used.

Fig. 4 shows the central region for four of the samples, the optical images are broadly similar in terms of light return level, and all show signs of surface pits/pores and remaining polishing scratches. The SRAS system can cope with this unevenness as this is below the roughness threshold (low arbitrary reflection). The velocity maps for the first three samples show similar properties, they have similar minimum/maximum velocities and the macrozone size and distribution is similar. However, for the 140W sample there is an obvious down shift in the velocity and a finer texture.

The velocity and acoustic amplitude for the sample set were recorded and plotted against build power. Fig. 5 shows that the velocity increases with build power; it can also be seen that the measurement is robust as the velocity measured does not vary with acoustic amplitude. This is to be expected, as long as there is sufficient signal to noise ratio, changes in the amplitude are not seen in the measured frequency (and hence the velocity). The acoustic amplitude for the 190 and 200W scans were similar to those of the lower build power scans but the measured velocity is quite different. The acoustic amplitude depends on both the generation conditions and the sample properties under the generation region, it also depends on the probe beam laser power and the amount of light returned to the detector. This means that the signal amplitude can vary across a single sample and also between different



**Fig. 4.** (top) A selection of optical maps and (bottom) velocity maps from the central region on the samples. Pores are present on all samples, the velocity variation is similar for the first 3 samples presented, and the 140 W sample shows a drop in mean velocity. Scale bar 0.5 mm.



**Fig. 5.** Average acoustic amplitude and velocity data presented for each SLM specimen. The velocity decreases with build power, and is not dependant on the acoustic amplitude as the 190 W and 200 W samples had similar acoustic amplitude to the lower power samples, yet there velocity was as expected for well consolidated material.

samples by quite a large factor. As SRAS uses the frequency, as long as the signal to noise is sufficient, any variation in amplitude is not seen in the recovered frequency making this a robust technique for measuring the acoustic velocity.

The velocity initially increases rapidly as the build power increases, (70–90W) then, although the velocity continues to increase with increasing build power, it does so at a reduced rate. The velocity eventually reaches a stable level for the higher build powers (160 W and above). There are several reasons why the velocity is affected. Firstly, the amount of porosity can be increasing. This essentially reduces the density of the material and increases the attenuation of the acoustic waves, but as it is on a much smaller scale than the wavelength of the acoustic waves it does not stop the propagation of the waves so they can still be measured. Secondly there can be changes to the texture of the material, for example, there can be a preferential grain growth direction which changes the distribution of the grain orientations. Thirdly, macroscopic pores can have an effect on the measured velocity and has been observed in these samples. For subsurface pores where the pore is larger than the acoustic wavelength and within an acoustic wavelength of the surface, the pore and acoustic wave interact; the

Rayleigh wave can undergo mode conversion to a different wave mode with a different acoustic velocity. In this case, it is proposed that the Rayleigh waves are converting to Lamb modes ( $A_0$ ) and this wave mode has a lower velocity. Fig. 6 shows a velocity scan where the velocity range has been expanded to allow the visualisation of the  $A_0$  mode. Here the texture of the material is no longer visible on this zoomed out scale but blue/yellow features around the location of possible pores are present. This mode conversion – resulting in a large localised reduction in the observed surface wave velocity – influences the mean velocity to a greater extent than could be attributed to the change in macroscopic density alone. This is particularly apparent for low build powers, where higher numbers of this type of defect are present. For the conducted SRAS scans, here, the wavelength and, hence, depth to which the SRAS system is sensitive to is  $\sim 25 \mu\text{m}$ .

### 3.2. Defect detection using SRAS instrument

Scans of the 190 W and 140 W samples with  $5 \mu\text{m}$  steps were performed to increase the number of points in the images to allow analysis of the pores that were seen in the samples.



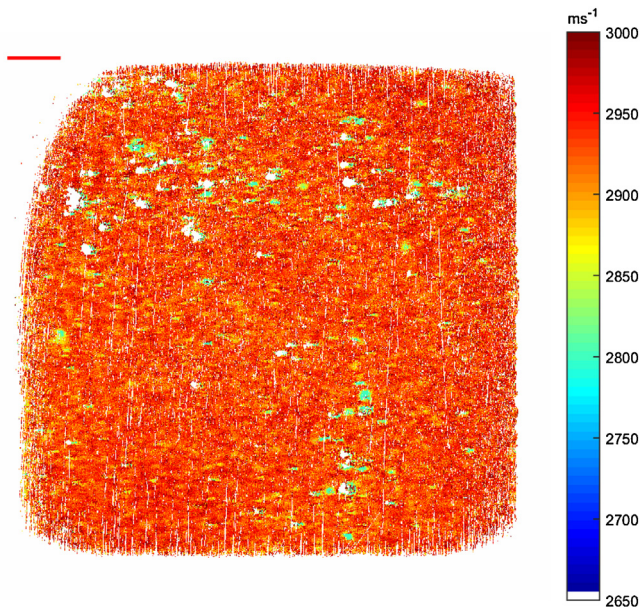


**Fig. 6.** Expanded velocity range image of the sample 10 (190 W). The texture of the material is lost as contrast is reduced, however yellow/green features can now be seen. These features have significantly lower velocity and are possibly due to mode conversion of the SAW into an A0 lamb mode at subsurface features. Scale bar 1 mm (for interpretation of the references to colour in this figure legend, the reader is referred to the web version of this article).

**Fig. 7(a)** shows the optical image obtained during the SRAS scan, here, despite being in the recommended input power zone for good build quality, many surface defects can be seen, the zoom in **(b)** shows a number of optical pores and also residual surface imperfections from the polishing can be seen. The surface preparation requirements are not very strict to obtain a good SRAS image, a mirror like polish is not required, the surface only needs to be shiny enough such that sufficient light returns to the detector and the reflection is mostly specular. **Fig. 7(c)** shows an SEM image of the surface showing that the surface defects seen in the optical images are pores with partly unfused powder within them (see inset), this is a well-known source of defects in SLM material. There is good agreement of the location of surface defects between the optical image and the SEM image. The SEM shows the defects in the surface have a size range of 20–150  $\mu\text{m}$ .

**Fig. 7(d)** shows the corresponding velocity image, the random variation of the velocity due to the texture of the material can be seen clearly. **Fig. 7(e)** shows the same zoomed area as in **(b)** there are several more regions where there is no signal (white regions) than for the optical image. As discussed earlier the velocity map is masked by the optical return level and the received acoustic amplitude. The white regions that do not have a corresponding dip in the optical image are therefore regions where there was sufficient reflection to have good data but where the acoustic waves were not detected. **Fig. 7(f)** shows an XCT image highlighting the pore locations just below the surface and shows good agreement with the location of features in the velocity map. These are not visible in the optical image. The differences between the optical and velocity map micrographs will be quantified in the pore detection section below.

**Fig. 8(a)** shows the difference between a thresholded optical image and a thresholded acoustic image. The image shows regions of invalid data, but not their values. By subtracting the acoustic image from the optical (optical is 0–2 range, acoustic is 0–1 range) four distinct cases can be observed.

- 1 If both maps have good data then the result is 0 (light blue).
- 2 If there is invalid optical data but good acoustic data then the result is 2 (red).
- 3 If there is invalid acoustic data but good optical data then the result is  $-1$  (dark blue).
- 4 If both have invalid data then the result is 1 (yellow).

From **Fig. 8(a)** no red data is observed, this is as expected, if there is no optical signal there cannot be an acoustic signal as the acoustic signal is carried by the optical signal. The yellow regions show that the location where there is bad optical data always corresponds to a pore in the acoustic data. Generally the dark blue regions surround a yellow regions – this is because the resolution of the acoustic data is lower than that of the optical signal ( $\sim 100$  vs  $\sim 5$   $\mu\text{m}$ ). The propagation direction of the waves can also be observed in the images as the acoustic pore data is biased to the right hand side of the optical pore location. This is due to the optical detection spot being offset from the generation patch as shown in **Fig. 1**.

Sub-surface pores can be seen across the sample; these are the dark blue regions without any yellow present. In this case there was enough light returning from the sample to suggest an acoustic signal should be measured but in these cases there was no acoustic data recorded, indicating something below the surface preventing the waves from reaching the probe beam. Presence of pores and their locations were confirmed with the XCT data, showing pores up to a depth of 2 SLM layers (60  $\mu\text{m}$ ).

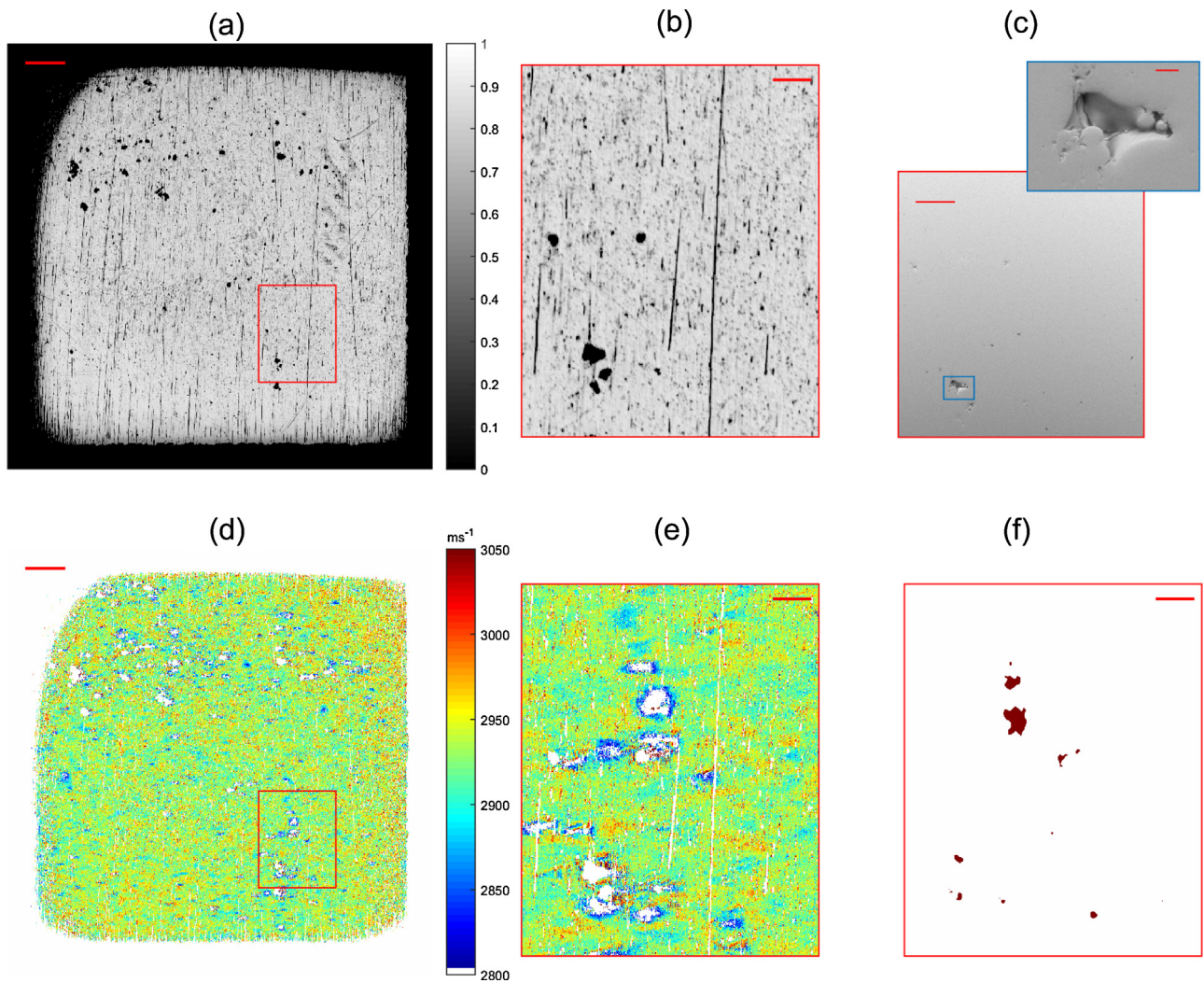
### 3.3. Automatic pore sizing algorithm

To look at the number and size of the features, and to compare the optical and acoustic response a simple algorithm to automatically find the features within the image was developed. This algorithm was written in Matlab<sup>®</sup> and made use of a number of standard image processing functions.

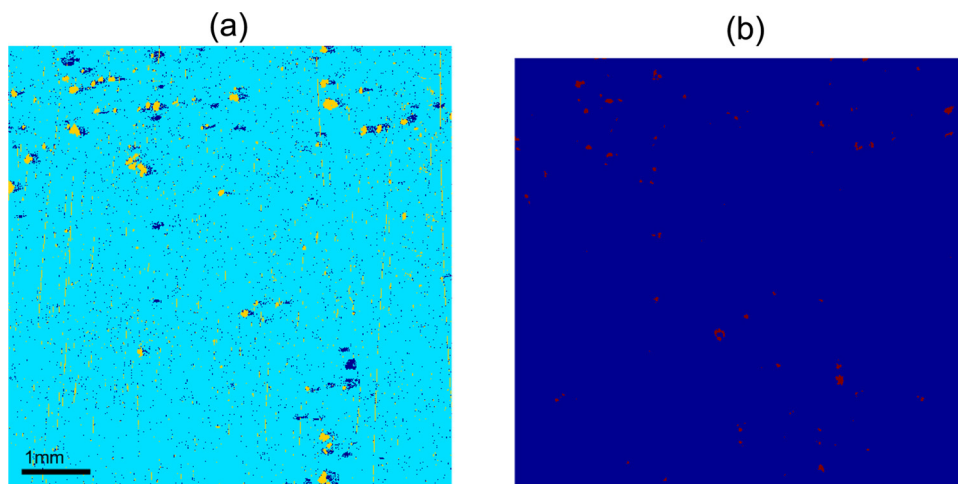
- 1 The thresholded optical and acoustic images were de-noised by eroding the small features, before dilating back to the original size.
- 2 An edge detection algorithm was used to find the edges of features.
- 3 The features were ‘dilated’ to close the gaps in the edges, then eroded to the original size.
- 4 The closed loops were then filled.
- 5 Any distinct area that was not background was then found, assigned a reference number and simple measurements were recorded, for example the area of the feature, the equivalent diameter of the feature, the eccentricity etc.

These measurements were then used to remove some unwanted features, for example, tool marks/scratches where their eccentricity is exceedingly high. This produces the maps shown in **Table 2**, which shows that the features found have a similar size and shape of the features in **Fig. 8(a)** and are also in close agreement with the location of subsurface features from the XCT data in **Fig. 8(b)**. The number of pores and the equivalent diameter for the two samples are also shown in **Table 2**.

As ideal melting powers of the SLM apparatus are  $\sim 190\text{W}$ , this sample was analysed as exhibiting good melting behaviour. For a contrasting measurement, the 140 W sample was scanned. From 190 W melting power to 140 W melting power the total pore count increases from 70 to 126 from the optical image data and 95–185 from the acoustic data. Due to the presence of subsurface pores in both samples, the acoustic pore count is higher than the optical data count. Interestingly, the mean pore diameter is about the same for both samples, which implies the number of pores is increasing but the pore size is not significantly changing. Also, as expected the

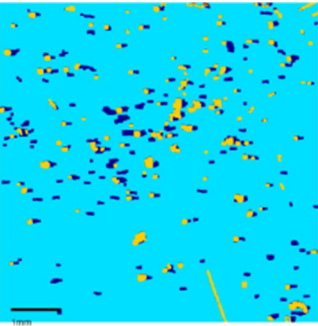
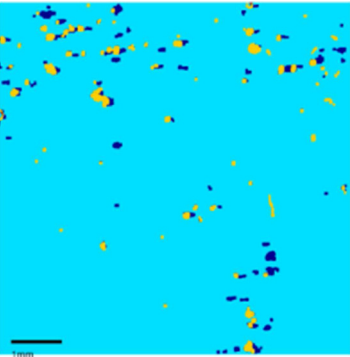


**Fig. 7.** Images for the 190 W AM test sample (a) Optical image (scale bar 1 mm) (b) Optical zoom (scale bar 250  $\mu\text{m}$ ), (c) SEM micrograph of the corresponding area (scale bar 250  $\mu\text{m}$ ) and inset zoom of large pore (scale bar 25  $\mu\text{m}$ ). (d) Acoustic velocity map (scale bar 1 mm) (e) zoom of acoustic data (scale bar 250  $\mu\text{m}$ ) (f) XCT subsurface (with no surface) data of zoomed region up to an approximate depth of 60  $\mu\text{m}$  (scale bar 250  $\mu\text{m}$ ).



**Fig. 8.** (a) Pore segmentation on optical and acoustic velocity scans of the 190 W sample; (b) XCT scan of the 190 W sample. For (a): red—optical pore only, blue—velocity pore only, light blue—no pores, yellow—both optical and velocity pores (for interpretation of the references to colour in this figure legend, the reader is referred to the web version of this article).

**Table 2**  
Pore size results from 140 W and 190 W samples.

SLM laser Power (W)	Difference Plot of Pores	Mean pore diameter ( $\mu\text{m}$ )	Standard Deviation of pore diameter	Total Pore Count
140W		115	44	126
		137	56	182
190W		119	47	70
		134	63	95

**Table 3**  
Main defects in metal powder based AM.

Metal Powder Bed Defect	Description	Typical sizes	Reference
Spherical pores	Entrapped gas pores within the bulk of the material. Material dependent.	min $\sim 9.9 \mu\text{m}$ (electron beam-PBF)	<a href="#">Tammam-Williams et al. (2015)</a> and <a href="#">Thijs et al. (2010)</a>
Acicular pores	Pores in between layers of the AM process.	min $5\text{--}20 \mu\text{m}$ (laser-PBF)	<a href="#">Tammam-Williams et al. (2015)</a> and <a href="#">Thijs et al. (2010)</a>
Unfused powder	The melt pool varies in size and unfused powder is present.	Satellite powder clumps: $100\text{--}150 \mu\text{m}$ .	<a href="#">Niu and Chang (1999)</a>
Cracking	Cracks can be within the component or a disconnection of the part from the baseplate is seen.	Parts on bed: residual stress in the range of materials yield strength.	<a href="#">Merzelis and Kruth (2006)</a> and <a href="#">Zaeh and Branner (2010)</a>

acoustic size of the pores is larger than its optical counterpart due to the lower resolution and shadowing effect discussed earlier. The sizes of the pores in the optical image agree well with those seen in the SEM image which is as expected as they are both very sensitive to the interaction of the measurement beam with changes in surface topography. The poor SNR of the XCT signal near the surface has meant that it has not been possible to have a direct comparison with the acoustic results; however the acoustic response has provided similar sizes to those of the optical signal for surface defects at locations that agree with the XCT data. Manufacturing known sized pores at specific locations is not possible for several reasons: Firstly, defects observed in SLM are in the order of magnitude of the powder sizes or low multiples thereof. Secondly, processing parameters have an uncontrolled influence on defect generation in that specific defect sizes at precise locations cannot be achieved by adapting the processing environment.

### 3.4. Towards online inspection

There are a number of challenges to overcome before online inspection with the SRAS instrument is possible. This covers inte-

gration of the instrument with the SLM production machine, overcoming the effects of surface roughness on the detection and generation of SAWs and ensuring that the inspection is fast enough so that the impact on the build time is kept to an acceptable level.

Currently, SLM machines are designed to house the build plate, powder feeder and recoater mechanism. Situated above the build plate, the f-theta lens enables the laser to enter the build chamber to melt the metal powder. This design does not incorporate space for the SRAS apparatus to be located close to the build plate for layer by layer investigation.

Furthermore, due to powder particulates (plume) being airborne within the build chamber manufacturers advise to clean the f-theta lens after each build and have developed jets of air that function to reduce the powder settling on the lens. A SRAS system would equally be subjected to those particulates if the optical train is situated within the build chamber.

The above mentioned restrictions can be eliminated by removing the SRAS instrument from the build chamber area and positioning it in the optical train of the laser melting system. Through a full integration, the translation of the measurement laser can be done by the already existing galvo system as it is in use for the



melting laser system. Since both the SLM and the SRAS are based on lasers, such integration could be an elegant solution without having to redesign SLM apparatus.

### 3.5. Roughness

The detector used in the SRAS instrument is a knife edge detector which can only operate well on samples with a roughness less than  $\sim 100$  nm  $R_a$ , as the detector requires a specular reflection from the sample surface. The as built SLM samples have a roughness of  $\sim 10$   $\mu\text{m}$   $R_a$ , which means that a different detector is required to work on unprepared surfaces. There are a number of optically rough surface detectors available; their suitability for integration into an SLM build platform is being investigated.

Surface roughness also impacts on the propagation of the generated acoustic waves; for very rough surfaces the waves will not propagate to the detection spot and therefore no measurement can be made. For surface waves the attenuation due to roughness scales with the 5th order of the frequency and so can become a significant issue at high frequencies. The propagation distance needed for SRAS is fortunately very small, typically  $\sim 200$   $\mu\text{m}$ , and so in the frequency range usually employed (10s' to 150 MHz) this has not yet been an issue.

Additionally, the problem of surface roughness is likely to diminish as SLM technology matures; roughness has already reduced considerably since the first generation machines were built, in part due to improvements in the control of the build parameters and also the reduction of powder sizes.

### 3.6. Scanning speed

In order for an inspection method to be viable for in-situ monitoring the time to perform an inspection of a layer needs to be considered. For the samples produced in this study, the melting laser spot of the SLM moved with a velocity  $600$   $\text{mms}^{-1}$ . The hatch spacing was  $75$   $\mu\text{m}$ . The resulting melting area per second of the SLM apparatus is  $45$   $\text{mm}^2\text{s}^{-1}$ . The processing time of the sample cubes can, hence, be calculated based on the  $10 \times 10 \times 10$  mm size. In order to determine the full processing time, the time of recoating needs to be incorporated. This is typically  $<4$  s and will be used for this investigation. For one of the sample parts, the SLM has fused 333 layers so the overall build time can be calculated to be 2072 s or 2.22 s per layer.

The SRAS scanning speed is dictated by the laser repetition rate, currently 2 kHz using a generation patch size of  $200$   $\mu\text{m}$  and with no oversampling, this gives the measured area per second to be  $80$   $\text{mm}^2\text{s}^{-1}$ , giving a layer measurement time of 1.25 s and a required translation speed of  $400$   $\text{mm/s}$  for the scan head. This is the ideal case where there is no allowance for any down time during the scan from, for example, acceleration and deceleration for direction changes. In the current scanning setup it takes roughly twice as long to scan as would be expected from the laser repetition rate due to the requirement to move the samples. In this more realistic case SRAS scans could be performed in a similar amount of time to the building of the layers. Additionally, there are lasers available with much higher repetition rates and similar pulse energies and pulse widths, using one of these lasers would give a  $\sim 10$  times increase in scanning speed. At these speeds scanning mirrors rather than scanning the instrument head would be required as the needed scan velocity becomes very large. At these speeds the inspection step would not cause any significant delays to the build time.

### 3.7. Measurement of defects

SRAS is able to measure the change in the acoustic velocity accurately. The measured velocity is related to a number of material parameters, the most important being density and elasticity. The density (Fleck and Smith, 1981) and elastic properties (Bache and Evans, 2001) are intrinsically linked to the parts integrity and performance; out of specification changes in either property can lead to premature part failure. Tracking changes in velocity, combined with the ability to quantitatively determine the number and size of near-surface pores, allows the monitoring of the AM process to ensure any loss of build control is known and introduces the possibility for remedial for action to be taken, e.g. scrap, rework or repair the build.

With regards to defects, the AM build process is susceptible to a number of different defect types, which are outlined in detail in Table 3, with circular pores with  $>5$   $\mu\text{m}$  sizes (Tammam-Williams et al., 2015), and acicular pores with  $50$ – $500$   $\mu\text{m}$  size ranges (Tammam-Williams et al., 2015; Zhou et al., 2015) being the most important with regards to the final parts performance. SRAS has been shown to be able to detect the presence of surface and sub-surface defects where the defect size is  $> \sim 50$   $\mu\text{m}$ . The limitations of SRAS with regards to defect detection have yet to be explored but the scalable nature of the resolution for this technique gives confidence that the capabilities of SRAS will cover a wide range of defect types and sizes. One limitation that is apparent from the data presented here is that the pore sizing is not possible when the pore density increases significantly. For high porosity samples the measured pores are no longer distinct and precise sizing becomes difficult. This means that SRAS will not be useful where high porosity material is being deliberately manufactured. While this may indeed be an intended application for users of additive manufacturing technology, far more prevalent at this time is a need for the analysis of solid features within parts.

## 4. Conclusions

It has been demonstrated that the surface acoustic wave velocity of the material changes with build power. It appears that if the build power is high enough to ensure full consolidation of the material then the velocity and the texture of the material is similar. However, as the build power reduces the velocity also starts to reduce and the texture appears to get finer.

The presence of pores in the surface from the SRAS optical images has been detected which is in good agreement with the SEM images. Additionally subsurface pores have been identified by analysis of the acoustic data obtained with the SRAS instrument and confirmed by XCT images up to a depth of  $\sim 25$   $\mu\text{m}$ . This in combination with fewer surface-pores visible shows that sub surface features of Ti-6Al-4V SLM samples can be detected with the SRAS.

The numbers of pores decreases with an increase in build power ( $126$ – $182$  to  $70$ – $92$  pores for  $10 \times 10$  mm scan area for  $140$  W and  $190$  W respectively). An increase in pores leads to an acceleration of the drop in acoustic velocity with lower build powers as mode conversion of the SAWs to Lamb modes has a large influence of the measured velocity. A lower average velocity indicates poor build quality of the SLM part.

While the data presented here was obtained offline and on prepared surfaces, the route to online inspection is feasible. Custom detectors will be used to detect the acoustic waves on unprepared surfaces. The scanning speed is already sufficient to not unduly hinder the build process. As the instrument utilising non-contact optical arrangement it could be combined with the SLM optical train to provide online monitoring of parts.

## Acknowledgements

This work is supported by the UK Research Centre in Non-Destructive Evaluation (RCNDE) under EP/L022125/1 and the Engineering and Physical Sciences Research Council (EPSRC). We would also like to thank our colleagues working on 'In-situ monitoring of component integrity during additive manufacturing Using Optical Coherence Tomography' (EP/L01713X/1) for the exchange of ideas working in similar fields.

## References

- Abe, F., Osakada, K., Shiomi, M., Uematsu, K., Matsumoto, M., 2001. The manufacturing of hard tools from metallic powders by selective laser melting. *J. Mater. Process. Technol.* 111, 210–213.
- Bache, M., Evans, W., 2001. Impact of texture on mechanical properties in an advanced titanium alloy. *Mater. Sci. Eng. A* 319, 409–414.
- Cerniglia, D., Scafidi, M., Pantano, A., Santospirito, S., 2013. Laser ultrasonic technique for laser powder deposition inspection. In: 13th Symposium of Non Destructive Characterisation of Materials, Le Mans, France.
- Clark, D., Sharples, S.D., Wright, D.C., 2011. Development of online inspection for additive manufacturing products. *Insight—Non-Destr. Test. Cond. Monit.* 53, 610–613 (614).
- Clijsters, S., Craeghs, T., Buls, S., Kempen, K., Kruth, J.P., 2014. In situ quality control of the selective laser melting process using a high-speed, real-time melt pool monitoring system. *Int. J. Adv. Manuf. Technol.* 75, 1089–1101.
- Fleck, N., Smith, R., 1981. Effect of density on tensile strength, fracture toughness, and fatigue crack propagation behaviour of sintered steel. *Powder Metall.* 24, 121–125.
- Islam, M., Purtonen, T., Piili, H., Salminen, A., Nyrhilä, O., 2013. Temperature profile and imaging analysis of laser additive manufacturing of stainless steel. *Phys. Procedia* 41, 835–842.
- Kruth, J.-P., Mercelis, P., Vaerenbergh, J.V., Froyen, L., Rombouts, M., 2005. Binding mechanisms in selective laser sintering and selective laser melting. *Rapid Prototyp. J.* 11.
- Kruth, J.-P., Mercelis, P., Vaerenbergh, J.V., Craeghs, T., 2007. Feedback control of Selective Laser Melting. <https://lirias.kuleuven.be/bitstream/123456789/185342/1/krufcs.pdf>.
- Li, W., Sharples, S.D., Smith, R.J., Clark, M., Somekh, M.G., 2012. Determination of crystallographic orientation of large grain metals with surface acoustic waves. *J. Acoust. Soc. Am.* 132, 738–745.
- Melchels, F.P.W., Domingos, M.A.N., Klein, T.J., Malda, J., Bartolo, P.J., Huttmacher, D.W., 2012. Additive manufacturing of tissues and organs. *Prog. Polym. Sci.* 37, 1079–1104.
- Mercelis, P., Kruth, J.-P., 2006. Residual stresses in selective laser sintering and selective laser melting. *Rapid Prototyp. J.* 12.
- Nemeth, J., Sears, J., Klein, M., 2005. Development of laser ultrasonics for defect detection during laser powder deposition. *Trends in Materials and Manufacturing Technologies for Transportation Industries and Powder Metallurgy Research and Development in the Transportation Industry as Held at the 2005 TMS Annual Meeting*, 33–39.
- Niebling, F., Otto, A., Geiger, M., 2002. Analyzing the DMLS-process by a macroscopic FE-model. *Proc. of 13th Solid Freeform Fabrication Symposium*, 5–7.
- Niu, H.J., Chang, I.T.H., 1999. Instability of scan tracks of selective laser sintering of high speed steel powder. *Scr. Mater.* 41, 1229–1234.
- Pavlov, M., Doubenskaia, M., Smurov, I., 2010. Pyrometric analysis of thermal processes in SLM technology. *Phys. Procedia* 5, 523–531.
- Rieder, H., Dillhöfer, A., Spies, M., Bamberg, J., Hess, T., 2014. Online monitoring of additive manufacturing processes using ultrasound. In: 11th European Conference on Non-Destructive Testing (ECNDT 2014), Prague, Czech Republic.
- Rudlin, J., Cerniglia, D., Scafidi, M., 2014. Inspection of laser powder deposited layers. In: 11th European Conference on Non-Destructive Testing (ECNDT 2014), Prague, Czech Republic.
- Sim, K.S., Kho, Y.Y., Tso, C.P., 2008. Application of contrast enhancement bilateral closing top-hat otsu thresholding (CEBICTOT) technique on crack images cybernetic intelligent systems, 2008. CIS 2008. 7th IEEE International Conference on, pp. 1–4.
- Simonelli, M., Tse, Y.Y., Tuck, C., 2014. On the texture formation of selective laser melted Ti-6Al-4V. *Metall. Mater. Trans. A* 45, 2863–2872.
- Smith, R.J., Li, W., Coulson, J., Clark, M., Somekh, M.G., Sharples, S.D., 2014. Spatially resolved acoustic spectroscopy for rapid imaging of material microstructure and grain orientation. *Meas. Sci. Technol.* 25, 055902.
- Tammas-Williams, S., Zhao, H., Léonard, F., Derguti, F., Todd, I., Prangnell, P.B., 2015. XCT analysis of the influence of melt strategies on defect population in Ti-6Al-4V components manufactured by selective electron beam melting. *Mater. Charact.* 102, 47–61.
- Tapia, G., Elwany, A., 2014. A review on process monitoring and control in metal-based additive manufacturing. *J. Manuf. Sci. Eng.* 136, 060801.
- Thijs, L., Verhaeghe, F., Craeghs, T., Humbeeck, J.V., Kruth, J.-P., 2010. A study of the microstructural evolution during selective laser melting of Ti-6Al-4V. *Acta Mater.* 58, 3303–3312.
- Voet, A., Mingneau, J., Dehaes, J., Kruth, J.-P., Vaerenbergh, v.J., 2005. Study of the wear behaviour of conventional and rapid tooling mould materials. In: *International Conference Polymers & Moulds Innovations PMI*, Gent, Belgium.
- Zaeh, M., Branner, G., 2010. Investigations on residual stresses and deformations in selective laser melting. *Prod. Eng. Res. Dev.* 4, 35–45.
- Zhou, X., Wang, D., Liu, X., Zhang, D., Qu, S., Ma, J., London, G., Shen, Z., Liu, W., 2015. 3D-imaging of selective laser melting defects in a Co-Cr-Mo alloy by synchrotron radiation micro-CT. *Acta Mater.* 98, 1–16.